This is the accepted version of the article. To cite this article, please refer to the published version:
Iakov Goldberg, Nirav Annavarapu, Simon Leitner, Karim Elkhouly, Fei Han, Niels Verellen, Tibor Kuna, Weiming Qiu, Cedric Rolin, Jan Genoe, Robert Gehlhaar, and Paul Heremans. 2023. *ACS Photonics* 10(5), 1591-1600. https://doi.org/10.1021/acsphotonics.3c00206

Multimode Lasing in All-Solution-Processed UV-Nanoimprinted Distributed Feedback $MAPbI_3$ Perovskite Waveguides

Iakov Goldberg[ab§*], Nirav Annavarapu[ab§], Simon Leitner[ac], Karim Elkhouly[ab], Fei Han[da], Niels Verellen[ad], Tibor Kuna[a], Weiming Qiu[ae], Cedric Rolin[a], Jan Genoe[ab], Robert Gehlhaar[a], and Paul Heremans[ab*]

AFFILIATIONS

[a]*IMEC, Kapeldreef 75, Leuven, 3001, Belgium*

[b]*ESAT, KU Leuven, Kasteelpark Arenberg, Leuven, 3001, Belgium*

[c]*MU Leoben, Franz-Josef-Straße 18, Leoben, 8700, Austria*

[d]*Department of Physics and Astronomy, KU Leuven, Celestijnenlaan 200D, Leuven, 3001, Belgium*

[e]*Department of Chemistry, KU Leuven, Celestijnenlaan 200F, Leuven, 3001, Belgium*

*Email: Iakov.Goldberg@imec.be; Paul.Heremans@imec.be

[§]*Iakov Goldberg and Nirav Annavarapu contributed equally to this paper*

ABSTRACT

In this work, we present an all-solution fabrication approach of external second-order 1D distributed feedback (DFB) gratings using soft UV-nanoimprint lithography (UV-NIL) above archetypical methylammonium lead iodide ($MAPbI_3$) perovskite films. This high-throughput method can be carried out in ambient environment and requires only slightly elevated temperatures as low as 70 °C, gentle imprint pressure, and the use of compatible UV-NIL resin. Under stripe-shaped optical excitation, we observe simultaneously occurring optical phenomena in our high-gain strong-scattering perovskite films, namely amplified spontaneous emission, random lasing, and 1D DFB lasing. In pursuit of distinguishing these mechanisms, we explore far-field emission patterns and output polarization. Additionally, the DFB lasing is hardly attenuated when a thin absorbing indium tin oxide (ITO) film, commonly used as an

electrode in fully contacted electrical devices, is inserted between the perovskite film and the DFB grating. As a result, we reproducibly achieve single- and multi-mode, low-threshold (below 100 $\mu J \cdot cm^{-2}$), narrow linewidth (below 0.2 nm), and strongly polarized (extinction ratio above 50) optically pumped DFB lasing for $MAPbI_3$ waveguides with and without an adjacent ITO layer. We believe that the proposed resonator integration approach can be extended toward complete electrically active devices, enabling an alternative integration scheme to achieve current-injection lasing.

KEYWORDS: metal halide perovskite, UV-NIL, perovskite lasers, distributed feedback lasers, cavity fabrication, cavity integration

Introduction

The unique optoelectronic properties of metal-halide perovskite semiconductors have enabled the rapid development of high-efficiency light-emitting devices. Owing to their rich chemistry,[1] long carrier lifetimes,[2] high charge carrier mobility[3] and optical gain values,[4] these materials are also widely explored as a lasing medium. To date, many different perovskite laser architectures have been reported such as whispering-gallery-mode,[5] Fabry–Perot,[6] distributed feedback (DFB),[7] vertical-cavity surface-emitting lasers,[8] etc.

To demonstrate low-threshold lasing, the development of fabrication methods for photonic perovskite sub-μm structures is necessary. Well-established lithography techniques rely on the extensive use of polar solvents that are not compatible with chemically fragile organic metal-halide perovskites.[9] In addition, temperatures as low as 85 °C can trigger thermally-activated decomposition of many of these perovskites even under inert conditions.[10] Thus, numerous less destructive perovskite patterning methods have been suggested in the literature. Perovskite film deposition atop pre-patterned substrates[11,12] or functional layers[13] is suitable to form the desired periodic nanostructures. In another approach, by virtue of their soft nature, perovskite films can be directly patterned by thermal nanoimprint lithography (T-NIL)[14,15] under high pressure at elevated temperatures. In particular, T-NIL combines direct surface texturing with thermal recrystallization that modifies the perovskite morphology and grain size.[14,16] However, the use of high imprint pressures (up to 900 bar)[17] and thermal heating cycles cause stamp wear that reduces the imprint quality, whereas long T-NIL cycle times (up to 40 min)[12,18] limit the attainable throughput.

In electrically active devices, the perovskite layer is sandwiched between other functional materials. Thin-film morphology is strongly dependent on processing techniques and can be modulated by the underlying layers. As a result, in multi-layered structures with embedded corrugations, thickness variations of deposited layers can lead to undesirable leakage currents,[13,19] strong local electric fields,[20]

and device instability.[21] To circumvent these limitations, a 1D DFB resonator can be placed external to the active region, e.g., above the perovskite. This enables index-coupling between the optical modes and a grating structure while maintaining a constant thickness of the active perovskite medium. A similar top-layer resonator configuration was demonstrated by placing polymer gratings, individually defined via e-beam lithography (EBL), above methylammonium lead bromide films.[22] A more scalable method was utilized for dye-doped organic polymers.[23,24] The patterns were transferred into photosensitive resist using water-based interference lithography, but this method is not applicable to organolead halide perovskites due to their instability towards water.[25]

Herein, we explore soft UV-nanoimprint lithography (UV-NIL) to manufacture high-density nanostructures directly atop archetypical spin-coated methylammonium lead iodide ($MAPbI_3$) perovskite films. UV-NIL offers several advantages over more traditional T-NIL. First, the use of a less viscous UV-curable resist eliminates the need for high imprint pressures, in contrast to those used in T-NIL.[26] The low viscosity of the curable resin reduces the time necessary for a pattern transfer,[27] and the transfer can be facilitated at room temperature. In contrast to the low-pressure T-NIL, which often requires tailoring of perovskite crystallization dynamics to achieve the desired imprint quality,[13,28] UV-NIL process conditions can be established independently. We show that commercially available UV-NIL products formulated with propylene glycol methyl ether acetate (PGMEA) solvent are suitable for a high-fidelity pattern transfer to perovskite-based optical lasers. We investigate the lasing properties of these 1D DFB perovskite lasers using stripe-shaped excitation beam. We remark that similar illumination conditions are efficient in guiding the random lasing (RL) emission even from the pristine non-imprinted perovskite films, and extensive investigations must be carried out to distinguish observed "look-alike" phenomena. We explore emission linewidth, stimulated emission threshold, polarization, and lasing mode patterns for different architectures. Moreover, we observe DFB lasing even when an absorbing indium tin oxide (ITO) film, commonly used as an electrode in fully contacted electrical

devices, is inserted between the perovskite film and the DFB grating. To explain the origin of multiple lasing peaks observed at pump fluences above the fundamental lasing mode threshold, we additionally employ a coupled mode theory simulation of the grating structure.[29] We expect that the UV-NIL resonator integration approach can be extended towards complete device stacks for injection lasing, and would advantageously result in an entirely planar electrical device structure with external DFB grating.

UV-NIL Fabrication Route

The fabrication flow of soft UV-NIL-imprinted 1D DFB perovskite lasers can be broken down into three distinctive steps (**Figure 1 a**). In the first step, a Si master template, which has the same pattern as the desired grating, is made using EBL patterning followed by dry etching. The master is coated with a fluorinated anti-sticking layer (ASL) to prevent the adhesion of the replication material. Then, the imprint patterns are transferred onto a flexible polyethylene terephthalate film via UV-assisted curing of the intermediate working stamp material. This working stamp, now featuring the inverted pattern of the Si master, is separated from the master template, concluding the working stamp fabrication. The Si stamp can be reused tens to hundreds of times as long as the quality of the ASL and etched features is not compromised.

In the third step, the working stamp pattern is gently laminated into a compatible UV-NIL photo-curable resin that is spin-coated above the ca. 110-nm-thick $MAPbI_3$ perovskite layer formed on a glass substrate. As-deposited perovskite films exhibit polycrystalline morphology with a root-mean-square roughness of 10.7 nm (**Supplementary Figure S1**). At the chosen perovskite thickness, amplified spontaneous emission (ASE) threshold is approaching a minimum, while also permitting a 12 % mode intensity overlap with the grating layer (**Supplementary Note S1**). There should be no chemical reaction between the UV-NIL resin and the perovskite. Following the results of a Hansen solubility analysis (**Supplementary Table S1**), we identify PGMEA as a promising organic solvent, with low environmental toxicity, to be used in the UV-NIL resin formulation. To improve the adhesion between

$MAPbI_3$ and the UV-NIL resin, thereby facilitating the final demolding, the perovskite can be first coated with isopropyl alcohol (IPA)-based adhesion promoter. To transfer the pattern into the UV-NIL resin, the working stamp features are laminated over the freshly deposited, uncured resin using gentle pressure with the NIL roller. The perovskite-resin assembly is then subjected to 100-second UVA irradiation at 100 $mW \cdot cm^{-2}$ (equivalent to AM 1.5G one sun), which converts the liquid UV-NIL resin into a cross-linked solid polymer. The working stamp is delaminated and can be immediately reused to transfer sub-μm features into the next perovskite device, which is an obvious throughput feature. In-depth fabrication details and a description of the used materials are provided in the **Experimental Methods** and **Supplementary Experimental Methods** sections.

The thickness of residual resist, i.e., a non-imprinted UV-NIL resin layer, is a function of the design pattern and its density, the initial thickness of the coated resist, fluidic properties of the resin, capillary forces, etc.[30] Typically, the initial thickness of the resin must be heuristically adjusted to achieve a minimum residual layer thickness. In our experiments, the resulting residual resin thickness after the imprint varied between 10 and 30 nm (**Figure 1 b**). The presence of a residual layer affects the waveguiding properties, namely the degree of mode overlap with the corrugated grating layer. On the other hand, the polymeric residual layer can act as an adequate encapsulation layer, protecting $MAPbI_3$ from excess water and oxygen permeation. Much thicker residual layers can further reduce the electric field intensity overlap with the grating layer, and thus should be avoided.[31]

Figures 1 b and **d** depict cross-sectional scanning electron microscopy (SEM) images of the UV-NIL imprinted perovskite waveguide taken at different tilt angles. The rounded grating profile originates from the initial Si master (**Supplementary Figure S2**). The up-close SEM images reveal the characteristic perovskite morphology. The lateral dimensions of the largest fabricated 1D DFB, which is used for the optical investigations in this work, are 140×40 μm^2 (**Figure 1 c**, bottommost structure). According to the atomic force microscopy (AFM) measurement displayed in **Figure 1 e**, the peak-to-

valley distance of the corrugated grating layer is approaching 80 ± 10 nm, as defined by the master mold. The periodicity of the second-order gratings under investigation is measured to be around 408 ± 5 nm while the grating duty cycle is around 45 %. The perovskite layer properties, all the DFB fabrication conditions, the grating layer periodicity, residual layer thickness, and other grating features remain fixed across this work.

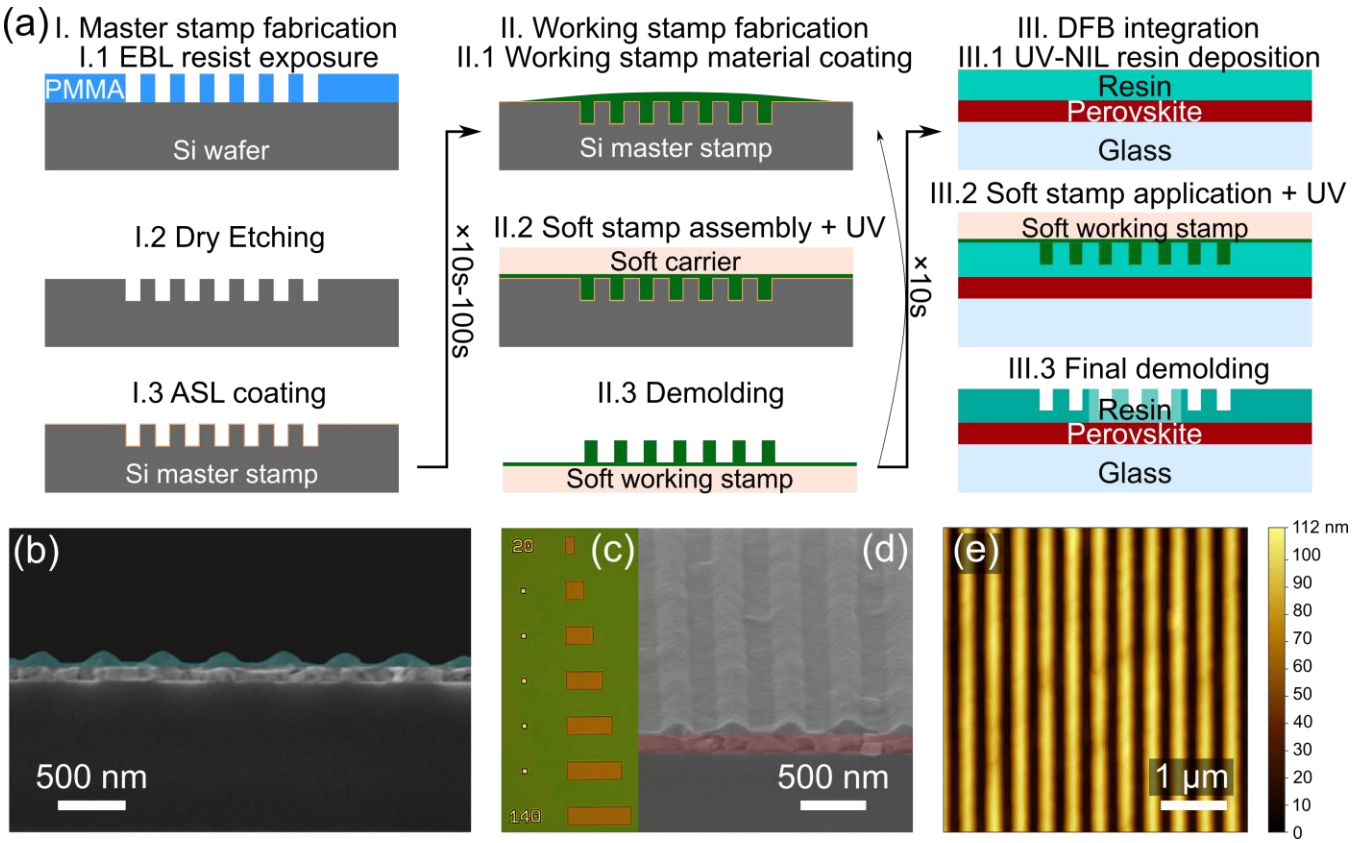

Figure 1. (a) UV-NIL fabrication approach, (b) cross-sectional SEM, (d) tilted cross-sectional SEM, and (e) AFM analyses of the fabricated resin/perovskite DFB grating. A UV-NIL resin layer in (b) is highlighted in cyan. A 110-nm-thick perovskite layer in (d) is highlighted in red. (c) Optical microscope image of the UV-NIL-imprinted DFB gratings above $MAPbI_3$. The studied grating dimensions are 140 × 40 μm^2 (lowest structure).

Optical Characterization

Unless otherwise stated, we employ a stripe excitation geometry to optically characterize various perovskite-based structures. In the case of imprinted UV-NIL resin-perovskite waveguides, the stripe excitation geometry promotes modes propagating perpendicular to the grating groves, thus preventing parasitic loss of gain through lateral ASE modes. The sample is illuminated from the glass side with a 532 nm, 3 ns, 20 Hz Q-switched laser. A uniform intensity profile is maintained along the stripe length, which is fixed at ≈ 140 μm. The Gaussian transverse stripe excitation profile is maintained at ≈ 24 μm FWHM. The pump energy is controlled by a combination of a variable neutral density filter and a polarizer. Photoluminescence (PL) is collected normal to the sample using a 50X magnification microscope system and is directed towards a spectrograph (HRS-500) coupled with an intensified CCD array detector. The CCD camera allows probing the spectra while preserving spatial information along one axis (parallel to the entrance slit of the spectrograph). To measure emitted mode polarization, a linear polarizer is placed between the microscope and the spectrometer. Far-field spectral images of the outcoupled emission from the gratings are obtained by introducing a Bertrand lens in the microscope system, thus revealing the angular distribution of light emitted normal to the sample.[32] The schematic of the setup and the pump beam spatial profiles are provided in **Supplementary Figure S3**.

Results and Discussion

First, we examine the PL properties of $MAPbI_3$ perovskite films covered by a plain UV-NIL resin layer, which are processed according to the proposed UV-NIL protocol without feature transfer. Significant reduction of the PL intensity or increase in ASE threshold in reference to bare perovskite films, characterized in **Supplementary Figure S4**, would be associated with chemical- or photodegradation,[33] had such occurred during the UV-NIL process steps, or with additional surface-roughness induced scattering losses coupled with a lower confinement factor of the mode in the gain volume.

Resin-coated perovskite films are excited with gradually increasing fluences I from 20 up to 220 μJ·cm^{-2} (**Figure 2 a**). PL evolves from a characteristic spontaneous emission (SE) with a fixed linewidth of ≈ 50 nm towards ASE at I_{th} = 78 μJ·cm^{-2}. A series of narrow lines, spanning the gain bandwidth, appear immediately after, which can be attributed to random lasing (RL). A random cavity can occur in any gain medium where light travels in a closed loop and accumulates an overall phase shift of $2\pi m$ after multiple scattering events. RL was observed both in perovskite thin films[34–36] and QDs.[37,38] In the case of polycrystalline films, RL strength could be manipulated by varying surface roughness,[36] morphology,[39] and even the underlying substrate.[40] RL forms in such cavities when the gain of the scattered mode overcomes the total radiation losses, and these modes are emitted in a speckle-like pattern.[41,42] RL peaks are randomly distributed within the gain bandwidth and vary significantly across different sample excitation positions over the sample.

Unlike ASE, RL modes are characterized by narrow spectral features down to FWHM of ≈ 0.3 nm (**Figure 2 b**). While new RL peaks appear at higher fluences, the spectral position of lower-threshold modes remains unchanged. A maximum polarization extinction of ≈ 11 was measured for an RL peak at 111 μJ·cm^{-2}, in contrast to ASE which should not have a distinct polarization direction.[43] The input-output intensity curve undergoes a superlinear transition from the SE regime to the stimulated emission regime above the threshold fluence (**Figure 2 c**).

Near-identical behavior is observed for the reference bare $MAPbI_3$ films on glass under stripe excitation (**Supplementary Figure S4**). Narrow RL modes emerge at I_{th} = 51 μJ·cm^{-2}, bypassing ASE. This eliminates the UV-NIL processing as a possible cause for the appearance of RL. Instead, the morphology of the layer and/or the stripe excitation geometry of the pump might be responsible for promoting RL. Our nanocrystalline $MAPbI_3$ films contain strong scattering sites while simultaneously possessing high optical gain. At first glance, our perovskite films display homogeneous morphology and minor thickness variations without apparent material voids, which cannot explain the random lasing

phenomenon. The exact origin of strong scattering centers requires further investigation, which is outside of the scope of this work.

In contrast to the stripe excitation, circular illumination (⌀ 400 µm) of the pristine $MAPbI_3$ film produces a smooth ASE signal, devoid of RL lines and with extinction reaching a mere 1.5 (**Supplementary Figure S5**). It is apparent that ASE and RL signals are present together in our system, and the excitation geometry determines the strength of each effect in the PL spectrum. A narrow-line excitation activates only a few random cavities, which may produce a dominant signal due to a higher closed-loop amplification. On the other hand, a large circular excitation volume permits multiple ASE modes, which reduce the available gain for random cavities, resulting in a stronger ASE signal than any individual closed-loop random cavity.

Upon imprinting 1D DFB gratings in UV-NIL resin, a periodic index perturbation in the waveguide is created which scatters guided modes internally. Lasing from such a structure is obtained when the internally scattered modes within the gain bandwidth form a standing wave that satisfies the Bragg condition ($\lambda_{DFB} = n_{eff}\Delta_{bragg}$). **Figure 2 d** shows lasing spectra obtained from the imprinted resin structure ($\Delta_{bragg} \approx 412$ nm) when excited using a stripe geometry perpendicular to the grating grooves. A clear ASE band becomes prevalent at I_{th} = 51 µJ·cm^{-2}. For the planar resin-perovskite waveguide, only scattered ASE within the numerical aperture (NA = 0.55) cone of the microscope objective reaches the spectrometer. In contrast, a grating can be very efficient in vertical ASE signal outcoupling.[44] Only at a higher excitation fluence of 94 µJ·cm^{-2}, a narrow peak appears which we attribute to DFB lasing. This trend suggests that ASE and DFB lasing co-exist within the film, and that the modal gain at the ASE threshold is insufficient to overcome imprinted grating reflection losses. Perovskite gain media may display similar thresholds for ASE and lasing, in particular for low-quality-factor 1D feedback structures.[44] The existence of very strong competing ASE or RL signals is considered undesirable as it depletes the density of inverted states,[45] thereby lowering the available gain coupled to the lasing mode.

The measured FWHM for the fundamental DFB lasing mode reaches ≈ 0.16 nm, corresponding to a cavity quality factor Q ($Q = \lambda/\lambda_{\mathrm{FWHM}}$) of ≈ 4900 (**Figure 2 e**). Similarly, very high Q factors were achieved in other external index-coupled perovskite DFBs, where the narrow linewidths were attributed to symmetry-protected bound states in the continuum.[22] Another notable feature of this mode is its very strong polarization, with an extinction ratio above 60. The recorded DFB lasing threshold is comparable to other optically-pumped second-order perovskite DFB lasers fabricated by various methods such as T-NIL, EBL, or via the deposition above a corrugated substrate (**Supplementary Table S2**). We note that excitation source parameters must be accounted for as they significantly influence the reported threshold values.[17] The longer pulses can impose thermal stress,[46] increasing the amplification threshold.

No other distinct narrow resonances show up until a pump fluence of 119 μJ·cm^{-2}. Above this fluence, additional spectral features emerge, whose origin is discussed later in the manuscript. In contrast to a planar waveguide that is dominated by RL, DFB lasing is characterized by a steeper growth of the stimulated emission signal, **Figure 2 f**. This indicates that the feedback introduced by the DFB grating enhances the process of stimulated emission above the threshold. Unlike the RL modes that are prone to chaotic spectral fluctuations of the lasing peaks when moving the excitation across the sample, 1D DFB grating modes are largely position-invariant. The measured DFB lasing wavelength shifts within ± 2 nm when probing different areas across the grating (**Supplementary Figure S6**). The variation can be primarily caused by imperfect grating feature replication in the resin, inherent to the UV-NIL process.

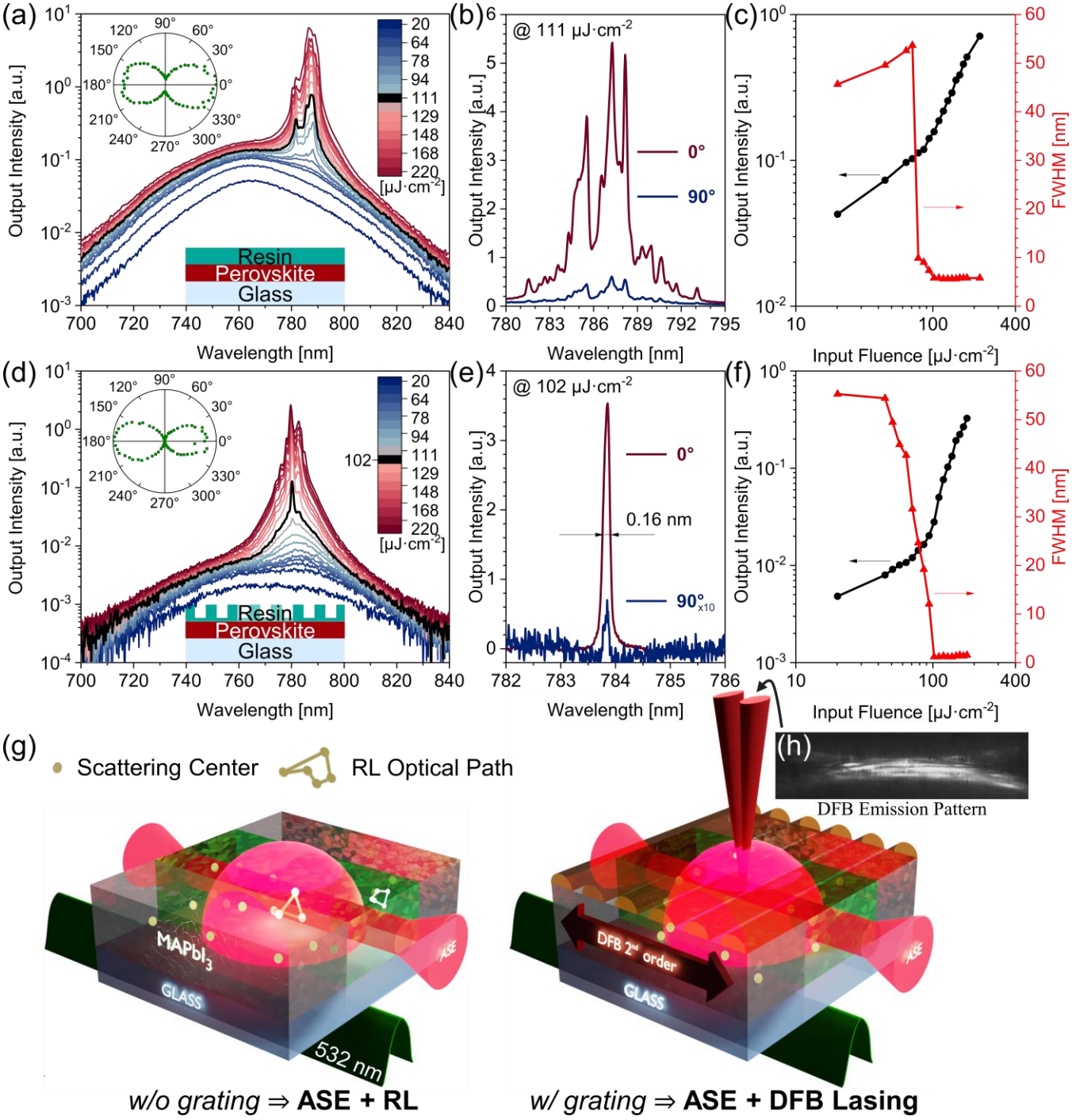

Figure 2. (a) PL spectra, (b) high-resolution emission spectra at 111 μJ·cm^{-2}, and (c) integrated PL output (black) and linewidth (red) for the slab resin/$MAPbI_3$/glass waveguide. The FWHM represents the linewidth of the corresponding ASE (Lorentzian) envelope. Inset in (a) depicts polarized emission output at 111 μJ·cm^{-2} with RL extinction reaching 11. (d) PL spectra, (e) high-resolution emission spectra at 102 μJ·cm^{-2}, and (f) integrated PL output (black) and linewidth (red) for the imprinted

resin/$MAPbI_3$/glass structure. The FWHM is provided for the ASE envelope and then for the fundamental DFB lasing mode at ≈ 784 nm. Inset in (d) depicts the intensity polar plot at 102 μJ·cm^{-2} with the DFB lasing extinction reaching 64. Note: 90° recording in (e) is scaled 10x for clarity. (g) Simplified schematic, depicting competing ASE, RL, and 1D DFB lasing mechanisms under the stripe excitation geometry. Dimensions are not to scale. (h) Fourier image of the imprinted DFB laser structure at 102 μJ·cm^{-2}.

This discussion suggests that three distinct phenomena (ASE, RL, and DFB lasing) compete in our strongly scattering perovskite films (**Figure 2 g**). The dominant mechanism is determined by the lowest loss mode and the highest *Q*-factor cavity. Without external feedback features, $MAPbI_3$ waveguides are dominated by the RL and ASE modes. Upon grating imprinting, DFB lasing and ASE modes define the emission output. However, we consider spectral features, rate of superlinear PL growth, and polarization data alone insufficient in contrasting these "look-alike" processes. DFB lasing can be verified by assessing the spatial coherence of emitted radiation as well-defined output beams.[47]

Second-order scattering from the grating grooves causes waveguided modes to be outcoupled at specific angles, depending on their effective index, relative to the sample normal.[28,48] Above the DFB lasing threshold, a homogeneous SE pattern transforms into an anisotropic beam with a very low divergence orthogonal to the grating grooves, and a large divergence along them (**Figure 2 h**).[47] Furthermore, this angular dispersion can be explored using a microscope fitted with a Bertrand lens to image far-field emission characteristics.[49] Lasing occurs when cavity modes fall within the gain bandwidth and the scattered mode momentum is zero, which corresponds to an outcoupled angle almost exactly normal to the surface.[48] The measured angular dispersion of a $MAPbI_3$ waveguide with the imprinted resin is shown in **Figure 3 a**, with intense lasing light being emitted close to the TE mode crossing. In addition, a non-negligible amount of DFB lasing light is scattered omnidirectionally. Low beam divergence (≈ 1.3° FWHM of the main lobes) and a sharp double-lobe far-field emission pattern are clear

indications of spatial coherence in our DFB laser.[50–52] The fitted lines show theoretical outcoupling angles of the waveguide modes when they interact with a periodic index perturbation of 412 nm, which match well with the structural DFB measurement. The measured ellipsometry data (**Supplementary Figure S7)** are incorporated into a model of the waveguide stack in Ansys Lumerical (**Supplementary Figure S8**). The effective indices of the fundamental guided TE and TM modes across multiple wavelengths are calculated using a Finite Difference Eigenmode solver.

A similar far-field measurement, performed on a planar resin-perovskite waveguide, shows no remarkable features in the angular domain (**Figure 3 b**). The recorded angular intensity in the microscope image of the outcoupled signal resembles a Lambertian emission profile (**Supplementary Note S2**). Thus, by examining far-field mode patterns, we can clearly distinguish 1D DFB grating-induced lasing from random lasing.

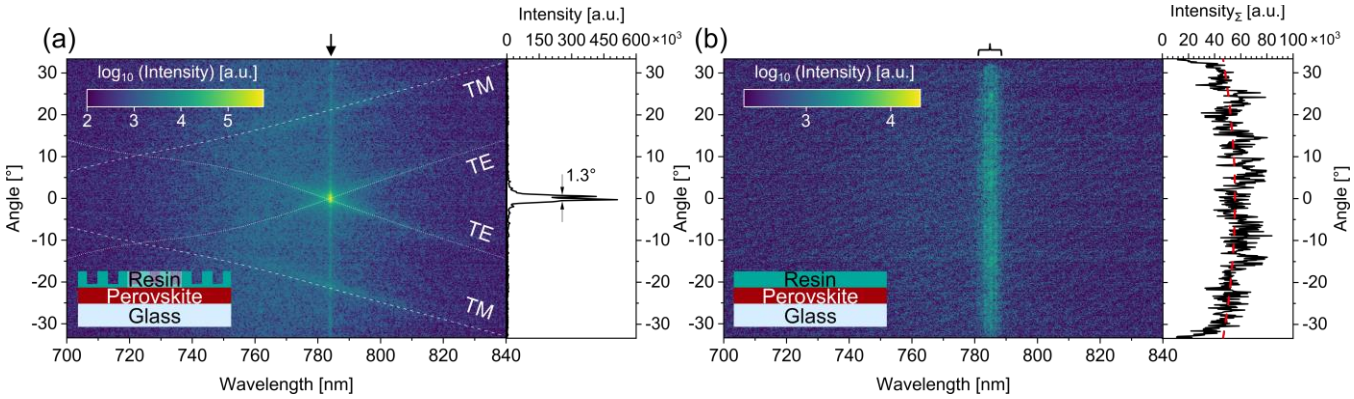

Figure 3. Angular spectrum of (a) 1D DFB-imprinted resin/$MAPbI_3$/glass structure as a function of wavelength and observation angle in *k*-space at 102 μJ·cm^{-2}. The angular cross-section in a cavity length direction features a double-lobe beam pattern, characteristic of the second-order surface-emitting 1D DFB, with a finite amount of astigmatism at ≈ 784 nm lasing wavelength (right, depicted by the black arrow). The objective NA restricts the detectable angular range to ± 33.3°. The fitted lines are calculated from the modal dispersion relations for the TE and TM modes. Angular spectrum of (b) planar resin/$MAPbI_3$/glass waveguide in *k*-space at 111 μJ·cm^{-2}. (Right) Angular cross-section, integrated over gain bandwidth, resembles a Lambertian far-field beam pattern (red dashed line).

We have demonstrated that UV-NIL can be utilized to fabricate sub-μm features directly above the standalone perovskite film on glass. Hereafter, we aim to assess whether this fabrication route can be extended to current-injection perovskite lasers. In a simplified scenario, such a functional electrical device would comprise an active perovskite gain layer surrounded by a pair of conductive electrodes. To maintain the planarity of an entire structure in line with this work, the grating can be integrated directly above the top electrode. This would further increase the optical separation between the waveguide modes originating in the perovskite gain layer and the external grating, reducing their coupling. On the other hand, a completely planar electrical architecture would benefit from the more uniform current injection that will yield a predictable and homogeneous gain profile.

Conventional highly conductive contact layers placed in close vicinity from a gain layer induce free-carrier optical absorption losses, resulting in a significant increase in the amplification threshold.[53,54] Therefore, an electrode (which also acts as an optical spacer) cannot be chosen arbitrarily. An example of a compatible electrode is a thin (20 nm) ITO layer, inserted directly in between the perovskite layer and the grating. The use of such a thin ITO layer is desirable to reduce absorption losses while also permitting higher mode overlap with the grating. The use of a similar thin ITO contacting scheme was widely explored for fully-contacted low-loss organic structures,[55–57] suggesting that this can be a viable solution for perovskite-based lasing devices. Not only can this transparent electrode inject charge carriers into the electrical device but also it can serve as an additional buffer layer to protect the perovskite layer against contact with undesirable UV-NIL chemistry.

Insertion of a thin ITO layer between the resin and $MAPbI_3$ results in a near-identical operation for this planar slab waveguide under stripe excitation, confirming no adverse influence of the electrode on the optical performance (**Supplementary Figure S9)**. The PL spectra extracted from the imprinted ITO stack are shown in **Figure 4 a**. Single narrow DFB lasing mode (FWHM ≈ 0.2 nm) emerges at a pump fluence close to 78 $\mu J \cdot cm^{-2}$, producing a polarization extinction of 58 (**Supplementary Figure S10)**.

The ITO stack, impressed with the same grating features as the ITO-free structure, displays DFB lasing upon optical pumping at a very similar wavelength. This can be attributed to a very small impact of the 20-nm ITO layer on the waveguide effective index. Additionally, process fluctuations introduced during the perovskite deposition and UV-NIL imprint may also result in slight thickness variability between the two stacks, tuning the resonant wavelengths closer to each other. Upon a further fluence increase, an additional lasing mode at ≈ 785.5 nm becomes visible (**Figure 4 b**). While the emission linewidths are similar for the two modes, the polarization extinction of the second mode (15:1) is weaker than that of the fundamental mode (51-58:1). On the other hand, polarization extinction of the higher-order mode is greater than the attenuation typically observed for RL modes. Thus, the second mode could either originate from a random cavity and have enhanced outcoupling due to the grating, or be a higher order DFB lasing mode supported by the grating, and distinguishing between the two phenomena is not trivial.

To study the cause of the second lasing peak, we perform two additional spectral measurements across the DFB grating at 86 $\mu J \cdot cm^{-2}$ (**Figure 4 c**). While RL produces sharp peaks at arbitrary wavelengths relative to the excitation position, higher-order DFB grating modes exist at specific wavelengths. At lasing threshold fluence, a single antisymmetric lasing mode should exist within the grating. Due to a low threshold gain margin, at higher fluences the waveguide gain increases, and a competing higher-order mode can be supported by the grating.[58] The spectral positions of these DFB lasing modes can be reproduced using a coupled mode simulation (elaborated in **Supplementary Note S3**).[29] The best fit is obtained by tuning the input parameters such as the effective indices, the grating length, period, and duty cycle. Importantly, the grating dimensions are set close to the experimentally measured values. The simulated lasing peak positions labeled "$Mode_{\pm 1}$" and "$Mode_{\pm 2}$" (centered around the photonic stop band) are placed above the measured multimode lasing peaks (**Figure 4 c**). The measured lasing spectral positions vary between the lowest threshold gain modes supported by the grating, and the dominant lasing mode is determined by the overlap of the intrinsic gain spectrum of the material and that of the

grating modes. The signal from a higher-order mode may dominate when local defects/scatterers in the grating modify the near-field intensity of the fundamental mode more strongly than that of the higher-order mode. Alternatively, it could be argued that the fluctuations in the lasing period could stem from nonuniformities or phase slips in the grating periodicity over the three probed locations. However, the lasing peaks observed in each of the three spectra consistently overlap with the simulated grating modes. Therefore, the existence of multiple lasing peaks at very similar wavelengths (supported by simulations) over different grating excitation positions suggests that we observe higher-order DFB lasing modes rather than RL outcoupled by the grating.

In addition, we examine the angular dispersion for the two modes at Position 1 at 86 $\mu J \cdot cm^{-2}$ (**Figure 4 d**). Intense lasing light is emitted close to the TE mode crossing, with characteristic mode patterns close to zero momentum. We note that a double-lobe pattern of Mode-$_1$ at this fluence cannot be resolved, while it clearly appears at 78 $\mu J \cdot cm^{-2}$ (**Supplementary Figure S10)**. A small angular deviation from the optimal excitation direction (i.e., perpendicular to the grating grooves) in this particular measurement or an insufficient angular resolution of our setup could be responsible for this.

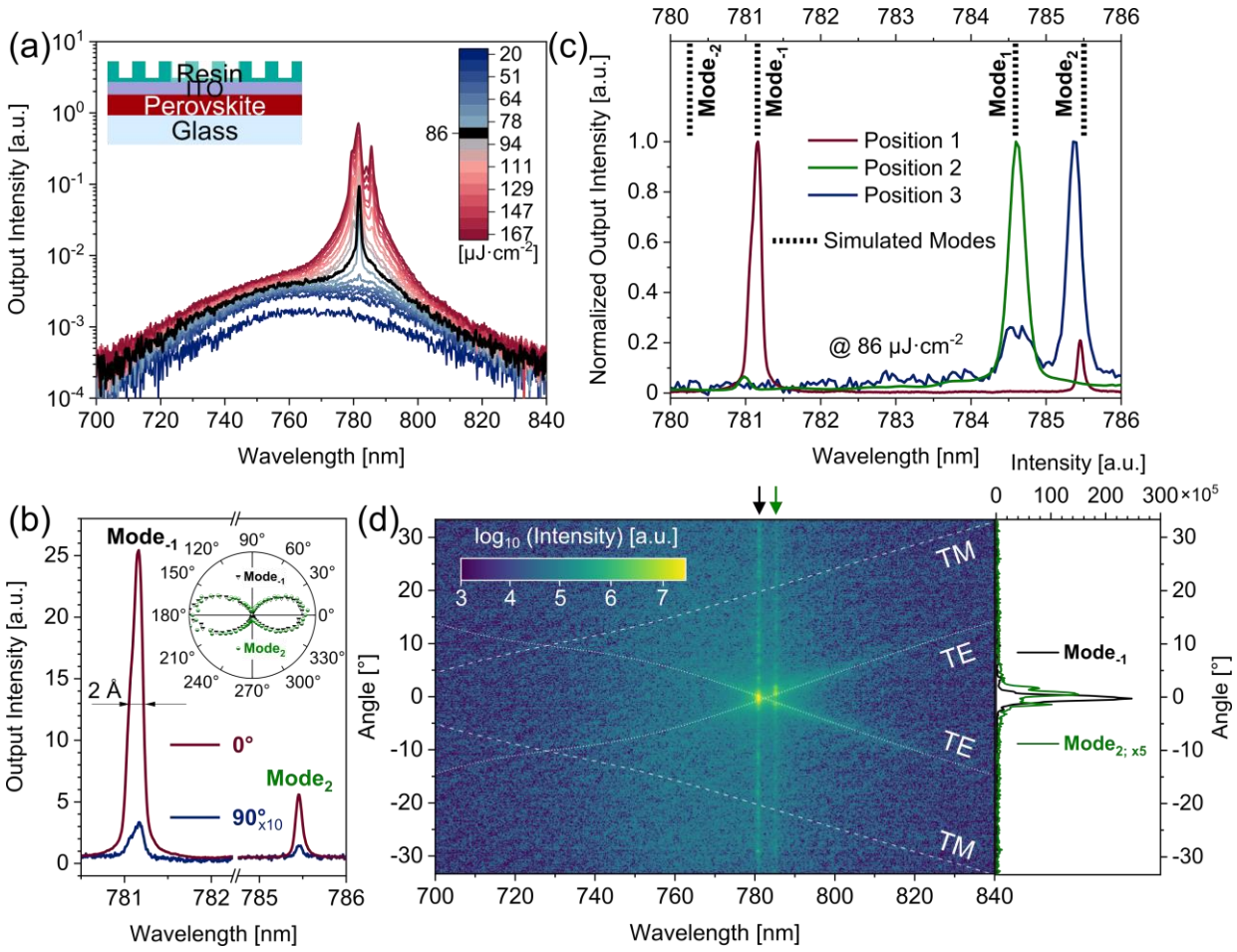

Figure 4. (a) PL spectra and (b) high-resolution emission spectra at 86 μJ·cm^{-2} for the imprinted resin/ITO/perovskite DFB on glass at Position 1. Inset in (b) depicts polarized emission output at 86 μJ·cm^{-2} for the fundamental mode at ≈ 781 nm and a higher-order mode at ≈ 785.5 nm with DFB lasing extinction reaching 51 and 15, respectively. (c) DFB lasing observed over the grating in three different locations at 86 μJ·cm^{-2}. The simulated mode positions are calculated based on coupled-mode equations. (d) Angular spectrum at a pump fluence of 86 μJ·cm^{-2} at Position 1. Note: Mode$_2$ cross-section in (d) is scaled 5x for clarity. The fitted lines are calculated from the modal dispersion relations at $\Delta_{bragg} \approx 404$ nm for the TE and TM modes.

By increasing the grating quality, reducing the thickness of the residual UV-NIL resin layer, optimizing the duty cycle, and engineering the grating depth or groove slopes it is possible to modulate the DFB feedback strength and reduce the lasing threshold.[31,59,60] In addition, a stronger coupling to the grating

can be achieved by employing a higher refractive index UV-NIL resin. Finally, we conclude that threshold and spectral analyses alone are insufficient to assert DFB lasing from the strongly scattering perovskite films. Using spatial coherence measurements and a coupled-mode theory, one can get a deeper insight into the origin of various spectral features. Unlike RL modes, DFB lasing peaks are characterized by minor spectral fluctuations when exciting different grating areas. Using this rigorous approach, we have demonstrated the capabilities of the UV-NIL technique to fabricate index-coupled 1D DFB lasing cavities above standalone $MAPbI_3$ films and above more complex multilayered electrode/$MAPbI_3$ structures. With the advantage of preserving the planarity of the fragile gain layer, UV-NIL can be further explored as a grating integration approach towards thin-film injection lasers.

Conclusions

In this work, we have proposed a novel all-solution soft UV-NIL processing approach to fabricate second-order 1D DFB optical lasers above archetypical $MAPbI_3$ perovskite gain layers. High optical gain coupled with the strong scattering properties of our perovskite films resulted in a significant PL signal dependence on the excitation geometry. For the narrow excitation stripes, the PL of the pristine and non-imprinted optical stacks was dominated by random lasing above the amplification threshold, superimposed on an amplified spontaneous emission Lorentzian envelope. Upon imprinting, DFB lasing was promoted in the films. To distinguish between the three co-existing phenomena, we analyzed far-field radiation patterns. Finally, we successfully applied the UV-NIL fabrication route to a more complex stack with an ITO interlayer between the planar perovskite layer and the imprinted UV-NIL resist. We investigated single mode and multimode lasing obtained from such a structure and employed coupled mode theory to differentiate between DFB and random lasing. The observation of DFB lasing from this structure reveals the potential of soft UV-NIL for the integration of optical feedback structures in more complex devices such as current-injection perovskite lasers.

Experimental Methods

Perovskite deposition. $MAPbI_3$ perovskite films were prepared under nitrogen atmosphere above glass substrates via one-step spin-coating. First, perovskite precursor salts MAI (CH_3NH_3I; Greatcell Solar Materials) and PbI_2 (TCI Chemicals) were mixed in equimolar proportion and dissolved in the N,N-dimethylformamide (DMF; Sigma-Aldrich) to obtain 1.2 M solution. The solution was further diluted by the addition of DMF to obtain ≈ 110-nm-thick perovskite film upon spin-coating. 50 µl of the final solution were spin-coated onto pre-cleaned glass substrates at 6000 rpm for 34 sec. The wet film was quenched by dropping 150 µl of toluene (Sigma-Aldrich) four seconds after the start of the spinning. Finally, annealing at 70 °C for five minutes was conducted to remove the excess solvent and to crystallize the film.

ITO sputtering. ITO (20 nm; 2 mTorr; $O_2/[O_2+Ar]$ flow ratio ≈ 3 %; deposition rate ≈ 2 $nm \cdot min^{-1}$) was DC-magnetron sputtered at mild conditions to reduce the bombardment impact on the perovskite layer. The substrate was kept at -5 °C during the deposition. The deposited ITO films are characterized by ≈ 600-800 $\Omega \cdot sq^{-1}$ sheet resistance.

UV-NIL fabrication. First, 1D DFB pattern was engraved into the Si master stamp using e-beam lithography and reactive ion etching. The Si stamp was coated with a fluorinated anti-sticking layer (ASL2-EVG; EV Group GmbH). Then, an intermediate flexible polymer stamp, bearing an inverse Si stamp pattern, was fabricated. UV-NIL resin was spin-coated at 3000 rpm and then annealed at 70 ºC for five minutes. The working stamp was employed to transfer the grating structures into the UV-NIL resin (PGMEA-based, EVGNIL UV/A3; EV Group GmbH), spin-coated above $MAPbI_3$ or ITO/$MAPbI_3$ structures. To improve the adhesion between $MAPbI_3$ and the resin, the perovskite or ITO was first coated with an IPA-based adhesion promoter (EVGPRIM K; EV Group GmbH) dynamically at 3000 rpm and annealed at 70 ºC for five minutes. The adhesion promoter and the UV-NIL resin were deposited under inert glovebox conditions. The thickness of the ASL layer is well below several nm and

was ignored in the optical simulations. The working stamp was brought in contact with a wet UV-NIL resin. Upon a 100-second flood exposure at 100 $mW \cdot cm^{-2}$ with the stamp still in place, the working stamp was carefully separated from the resin, completing the external UV-NIL 1D DFB fabrication. These last steps were conducted in an ambient cleanroom environment with a relative humidity of 43 %. Additional UV-NIL processing details are located in the **Supplementary Experimental Methods** section.

Optical and structural measurements. ASE and lasing performance were characterized using a Q-switched laser (CryLaS FTSS 355-300, 3 ns in FWHM, 20 Hz), which produces frequency-doubled pulses at 532 nm wavelength. The PL emerging from the sample was imaged by a microscope equipped with a Mitutoyo 50X infinity corrected objective (f = 4 mm), coupled with a tube lens (f = 200 mm). The imaged PL was focused on the entrance of an imaging spectrometer (Teledyne Princeton Instruments SpectraPro HRS-500), and the spectra were recorded using a digital intensified camera (Teledyne Princeton Instruments PI-MAX 4 with a spectral resolution of 0.03 nm). To obtain far-field images, a Bertrand lens (f = 150 mm) was added to the microscope beam path. Optical characterization was carried out in the ambient environment without additional encapsulation. No deterioration of optical performance was observed under these measurement conditions. The schematic of the optical experimental setup is shown in **Supplementary Figure S3.** Cross-sectional SEM images were obtained using the FEI Nova 200 scanning electron microscope system. SEM specimens were cleaved from the identical devices with Si/SiO_2 as an underlying substrate. AFM images were produced using a Bruker Dimension Edge system in a tapping mode to evaluate the film morphology and the UV-NIL imprint quality. AFM measurements were conducted in air. The thicknesses and the n/k coefficients of the employed films were extracted using spectroscopic ellipsometry measurements (RC2, J.A.Woollam).

Optical simulations. To extract the resonance spectrum of the 1D DFB laser and the electric field intensity distribution within the structure **(Supplementary Figure S8)**, finite-difference time-domain

simulations in Ansys Lumerical were performed. A single period of the grating structure was excited by a broadband TE dipole, and periodic boundary conditions were applied along the waveguide to simulate infinite periods.

To simulate theoretical outcoupling angles, which were fit to the far-field images, the effective index of the average waveguide structure over one period was calculated using a Finite Difference Eigenmode solver in Ansys Lumerical. The mode momentum and mode outcoupling angles were calculated using the TE and TM effective indices.[48] To model the DFB laser resonances, a custom python code was written to solve the coupled wave equations.[61]

Supporting Information

Supporting Information Available: complete UV-NIL fabrication details; Hansen solubility theory analysis; setup schematics; additional optical and structural measurements; spectroscopic ellipsometry measurements; simulation snapshots; additional discussion notes (PDF). This material is available free of charge via the Internet at http://pubs.acs.org.

Funding Sources

The authors acknowledge funding from the European Research Council under the European Horizon 2020 Programme/ERC grant agreement no. 835133 (ULTRA-LUX).

Notes

The authors declare no competing financial interest.

ACKNOWLEDGEMENTS

The authors thank Prof. dr. Nicolas Le Thomas from Ghent University for his input on far-field measurements.

DATA AVAILABILITY STATEMENT

The data that support the findings of this study are available from the corresponding authors upon reasonable request.

CORRESPONDING AUTHORS

Iakov Goldberg, e-mail: Iakov.Goldberg@imec.be.

Paul Heremans, e-mail: Paul.Heremans@imec.be.

AUTHOR CONTRIBUTIONS

Iakov Goldberg and Nirav Annavarapu contributed equally to this work. The manuscript was written through contributions of all authors. All authors have given approval to the final version of the manuscript.

REFERENCES

(1) Quan, L. N.; Rand, B. P.; Friend, R. H.; Mhaisalkar, S. G.; Lee, T. W.; Sargent, E. H. Perovskites for Next-Generation Optical Sources. *Chemical Reviews* **2019**, *119* (12), 7444–7477. https://doi.org/10.1021/acs.chemrev.9b00107.

(2) Miyata, K.; Atallah, T. L.; Zhu, X. Y. Lead Halide Perovskites: Crystal-Liquid Duality, Phonon Glass Electron Crystals, and Large Polaron Formation. *Science Advances* **2017**, *3* (10), 1–11. https://doi.org/10.1126/sciadv.1701469.

(3) Wang, Y.; Zhang, Y.; Zhang, P.; Zhang, W. High Intrinsic Carrier Mobility and Photon Absorption in the Perovskite CH3NH3PbI3. *Physical Chemistry Chemical Physics* **2015**, *17* (17), 11516–11520. https://doi.org/10.1039/c5cp00448a.

(4) Zhang, Q.; Su, R.; Du, W.; Liu, X.; Zhao, L.; Ha, S. T.; Xiong, Q. Advances in Small Perovskite-Based Lasers. *Small Methods* **2017**, *1* (9), 1–12. https://doi.org/10.1002/smtd.201700163.

(5) Zhang, Q.; Ha, S. T.; Liu, X.; Sum, T. C.; Xiong, Q. Room-Temperature near-Infrared High-Q Perovskite Whispering-Gallery Planar Nanolasers. *Nano Letters* **2014**, *14* (10), 5995–6001. https://doi.org/10.1021/nl503057g.

(6) Zhu, H.; Fu, Y.; Meng, F.; Wu, X.; Gong, Z.; Ding, Q.; Gustafsson, M. V.; Trinh, M. T.; Jin, S.; Zhu, X. Y. Lead Halide Perovskite Nanowire Lasers with Low Lasing Thresholds and High Quality Factors. *Nature Materials* **2015**, *14* (6), 636–642. https://doi.org/10.1038/nmat4271.

(7) Qin, C.; Sandanayaka, A. S. D.; Zhao, C.; Matsushima, T.; Zhang, D.; Fujihara, T.; Adachi, C. Stable Room-Temperature Continuous-Wave Lasing in Quasi-2D Perovskite Films. *Nature* **2020**, *585* (7823), 53–57. https://doi.org/10.1038/s41586-020-2621-1.

(8) Huang, C. Y.; Zou, C.; Mao, C.; Corp, K. L.; Yao, Y. C.; Lee, Y. J.; Schlenker, C. W.; Jen, A. K. Y.; Lin, L. Y. CsPbBr3 Perovskite Quantum Dot Vertical Cavity Lasers with Low Threshold and High Stability. *ACS Photonics* **2017**, *4* (9), 2281–2289. https://doi.org/10.1021/acsphotonics.7b00520.

(9) Lin, C. H.; Zeng, Q.; Lafalce, E.; Yu, S.; Smith, M. J.; Yoon, Y. J.; Chang, Y.; Jiang, Y.; Lin, Z.; Vardeny, Z. V.; Tsukruk, V. V. Large-Area Lasing and Multicolor Perovskite Quantum Dot Patterns. *Advanced Optical Materials* **2018**, *6* (16), 1–9. https://doi.org/10.1002/adom.201800474.

(10) Conings, B.; Drijkoningen, J.; Gauquelin, N.; Babayigit, A.; D'Haen, J.; D'Olieslaeger, L.; Ethirajan, A.; Verbeeck, J.; Manca, J.; Mosconi, E.; De Angelis, F.; Boyen, H. G. Intrinsic Thermal Instability of Methylammonium Lead Trihalide Perovskite. *Advanced Energy Materials* **2015**, *5* (15), 1–8. https://doi.org/10.1002/aenm.201500477.

(11) Hu, J.; Xue, H.; Zhang, X. Two-Dimensional Crystalline Gridding Networks of Hybrid Halide Perovskite for Random Lasing. *Crystals* **2021**, *11* (9), 1–9. https://doi.org/10.3390/cryst11091114.

(12) Pourdavoud, N.; Haeger, T.; Mayer, A.; Cegielski, P. J.; Giesecke, A. L.; Heiderhoff, R.; Olthof, S.; Zaefferer, S.; Shutsko, I.; Henkel, A.; Becker-Koch, D.; Stein, M.; Cehovski, M.; Charfi, O.; Johannes, H. H.; Rogalla, D.; Lemme, M. C.; Koch, M.; Vaynzof, Y.; Meerholz, K.; Kowalsky, W.; Scheer, H. C.; Görrn, P.; Riedl, T. Room-Temperature Stimulated Emission and Lasing in Recrystallized Cesium Lead Bromide Perovskite Thin Films. *Advanced Materials* **2019**, *31* (39). https://doi.org/10.1002/adma.201903717.

(13) Kim, H.; Roh, K.; Murphy, J. P.; Zhao, L.; Gunnarsson, W. B.; Longhi, E.; Barlow, S.; Marder, S. R.; Rand, B. P.; Giebink, N. C. Optically Pumped Lasing from Hybrid Perovskite Light-Emitting

Diodes. *Advanced Optical Materials* **2020**, *8* (1), 3–9. https://doi.org/10.1002/adom.201901297.

(14) Mayer, A.; Buchmüller, M.; Wang, S.; Steinberg, C.; Papenheim, M.; Scheer, H.-C.; Pourdavoud, N.; Haeger, T.; Riedl, T. Thermal Nanoimprint to Improve the Morphology of MAPbX 3 (MA = Methylammonium, X = I or Br) . *Journal of Vacuum Science & Technology B, Nanotechnology and Microelectronics: Materials, Processing, Measurement, and Phenomena* **2017**, *35* (6), 06G803. https://doi.org/10.1116/1.4991619.

(15) Pourdavoud, N.; Wang, S.; Mayer, A.; Hu, T.; Chen, Y.; Marianovich, A.; Kowalsky, W.; Heiderhoff, R.; Scheer, H. C.; Riedl, T. Photonic Nanostructures Patterned by Thermal Nanoimprint Directly into Organo-Metal Halide Perovskites. *Advanced Materials* **2017**, *29* (12), 1–6. https://doi.org/10.1002/adma.201605003.

(16) Schmager, R.; Hossain, I. M.; Schackmar, F.; Richards, B. S.; Gomard, G.; Paetzold, U. W. Light Coupling to Quasi-Guided Modes in Nanoimprinted Perovskite Solar Cells. *Solar Energy Materials and Solar Cells* **2019**, *201* (May), 110080. https://doi.org/10.1016/j.solmat.2019.110080.

(17) Allegro, I.; Bonal, V.; Mamleyev, E. R.; Villalvilla, J. M.; Quintana, J. A.; Jin, Q.; Díaz-García, M. A.; Lemmer, U. Distributed Feedback Lasers by Thermal Nanoimprint of Perovskites Using Gelatin Gratings. *ACS Applied Materials & Interfaces* **2023**, *15* (6), 8436–8445. https://doi.org/10.1021/ACSAMI.2C22920.

(18) Moon, J.; Alahbakhshi, M.; Gharajeh, A.; Li, Q.; Li, Z.; Haroldson, R.; Kwon, S.; Hawkins, R.; Kim, M. J.; Hu, W.; Zhang, X.; Zakhidov, A.; Gu, Q. Quasi-CW Lasing from Directly Patterned and Encapsulated Perovskite Cavity at 260 K. *ACS Photonics* **2022**, *9* (6), 1984–1991. https://doi.org/10.1021/acsphotonics.2c00071.

(19) Xu, K.; Lu, C.; Huang, Y.; Hu, J.; Wang, X. Enhanced Outcoupling Efficiency and Removal of the Microcavity Effect in Top-Emitting OLED by Using a Simple Vapor Treated Corrugated Film. *RSC Advances* **2017**, *7* (86), 54876–54880. https://doi.org/10.1039/c7ra11384f.

(20) Jeong, S. M.; Araoka, F.; Machida, Y.; Takanishi, Y.; Ishikawa, K.; Takezoe, H.; Nishimura, S.; Suzaki, G. Enhancement of Light Extraction from Organic Light-Emitting Diodes with Two-Dimensional Hexagonally Nanoimprinted Periodic Structures Using Sequential Surface Relief Grating. *Japanese Journal of Applied Physics* **2008**, *47* (6 PART 1), 4566–4571. https://doi.org/10.1143/JJAP.47.4566.

(21) Kim, D.; Ha, J.; Park, J.; Hwang, J.; Jeon, H.; Lee, C.; Hong, Y. Enhanced Light Outcoupling of Polymer Light-Emitting Diodes with a Solution-Processed, -Flattening Photonic-Crystal Underlayer. *Journal of Information Display* **2016**, *17* (4), 143–150. https://doi.org/10.1080/15980316.2016.1219404.

(22) Wang, Y.; Fan, Y.; Zhang, X.; Tang, H.; Song, Q.; Han, J.; Xiao, S. Highly Controllable Etchless Perovskite Microlasers Based on Bound States in the Continuum. *ACS Nano* **2021**, *15* (4), 7386–7391. https://doi.org/10.1021/acsnano.1c00673.

(23) Zhai, T.; Zhang, X.; Pang, Z. Polymer Laser Based on Active Waveguide Grating Structures. *Optics Express* **2011**, *19* (7), 6487. https://doi.org/10.1364/oe.19.006487.

(24) Quintana, J. A.; Villalvilla, J. M.; Morales-Vidal, M.; Boj, P. G.; Zhu, X.; Ruangsupapichat, N.; Tsuji, H.; Nakamura, E.; Díaz-García, M. A. An Efficient and Color-Tunable Solution-Processed Organic Thin-Film Laser with a Polymeric Top-Layer Resonator. *Advanced Optical Materials* **2017**, *5* (19), 1–9. https://doi.org/10.1002/adom.201700238.

(25) Crespo-Quesada, M.; Pazos-Outón, L. M.; Warnan, J.; Kuehnel, M. F.; Friend, R. H.; Reisner, E.

Metal-Encapsulated Organolead Halide Perovskite Photocathode for Solar-Driven Hydrogen Evolution in Water. *Nature Communications* **2016**, *7*, 6–12. https://doi.org/10.1038/ncomms12555.

(26) U. Plachetka; Bender, M.; Fuchs, A.; Vratzov, B.; Glinsner, T.; Lindner, F.; Kurz, H. Wafer Scale Patterning by Soft UV-Nanoimprint Lithography. *Microelectronic Engineering* **2004**, *73–74*, 167–171. https://doi.org/10.1016/j.mee.2004.02.035.

(27) Vogler, M.; Wiedenberg, S.; Mühlberger, M.; Bergmair, I.; Glinsner, T.; Schmidt, H.; Kley, E. B.; Grützner, G. Development of a Novel, Low-Viscosity UV-Curable Polymer System for UV-Nanoimprint Lithography. *Microelectronic Engineering* **2007**, *84* (5–8), 984–988. https://doi.org/10.1016/j.mee.2007.01.184.

(28) Dong, Q.; Fu, X.; Seyitliyev, D.; Darabi, K.; Mendes, J.; Lei, L.; Chen, Y.-A.; Chang, C.-H.; Amassian, A.; Gundogdu, K.; So, F. Cavity Engineering of Perovskite Distributed Feedback Lasers. *ACS Photonics* **2022**, *9* (9), 3124–3133. https://doi.org/10.1021/acsphotonics.2c00917.

(29) Kogelnik, H.; Shank, C. V. Coupled-Wave Theory of Distributed Feedback Lasers. *Journal of Applied Physics* **1972**, *43* (5), 2327–2335. https://doi.org/10.1063/1.1661499.

(30) Thanner, C.; Eibelhuber, M. UV Nanoimprint Lithography: Geometrical Impact on Filling Properties of Nanoscale Patterns. *Nanomaterials* **2021**, *11* (3). https://doi.org/10.3390/nano11030822.

(31) Huang, W.; Shen, S.; Pu, D.; Wei, G.; Ye, Y.; Peng, C.; Chen, L. Working Characteristics of External Distributed Feedback Polymer Lasers with Varying Waveguiding Structures. *Journal of Physics D: Applied Physics* **2015**, *48* (49). https://doi.org/10.1088/0022-3727/48/49/495105.

(32) Vasista, A. B.; Sharma, D. K.; Kumar, G. V. P. Fourier Plane Optical Microscopy and

Spectroscopy. *digital Encyclopedia of Applied Physics* **2019**, 1–14. https://doi.org/10.1002/3527600434.EAP817.

(33) Niu, G.; Guo, X.; Wang, L. Review of Recent Progress in Chemical Stability of Perovskite Solar Cells. *Journal of Materials Chemistry A* **2015**, *3* (17), 8970–8980. https://doi.org/10.1039/C4TA04994B.

(34) Chirvony, V. S.; Suárez, I.; Sanchez-Diaz, J.; Sánchez, R. S.; Rodríguez-Romero, J.; Mora-Seró, I.; Martínez-Pastor, J. P. Unusual Spectrally Reproducible and High Q-Factor Random Lasing in Polycrystalline Tin Perovskite Films. *Advanced Materials* **2023**. https://doi.org/10.1002/adma.202208293.

(35) Dhanker, R.; Brigeman, A. N.; Larsen, A. V.; Stewart, R. J.; Asbury, J. B.; Giebink, N. C. Random Lasing in Organo-Lead Halide Perovskite Microcrystal Networks. *Applied Physics Letters* **2014**, *105* (15). https://doi.org/10.1063/1.4898703.

(36) Safdar, A.; Wang, Y.; Krauss, T. F. Random Lasing in Uniform Perovskite Thin Films. *Optics Express* **2018**, *26* (2), A75. https://doi.org/10.1364/OE.26.000A75.

(37) Yakunin, S.; Protesescu, L.; Krieg, F.; Bodnarchuk, M. I.; Nedelcu, G.; Humer, M.; De Luca, G.; Fiebig, M.; Heiss, W.; Kovalenko, M. V. Low-Threshold Amplified Spontaneous Emission and Lasing from Colloidal Nanocrystals of Caesium Lead Halide Perovskites. *Nature Communications* **2015**, *6*. https://doi.org/10.1038/ncomms9056.

(38) Wang, L.; Yang, M.; Zhang, S.; Niu, C.; Lv, Y. Perovskite Random Lasers, Process and Prospects. *Micromachines* **2022**, *13* (12). https://doi.org/10.3390/mi13122040.

(39) Kao, T. S.; Chou, Y. H.; Hong, K. Bin; Huang, J. F.; Chou, C. H.; Kuo, H. C.; Chen, F. C.; Lu, T. C. Controllable Lasing Performance in Solution-Processed Organic-Inorganic Hybrid Perovskites.

Nanoscale **2016**, *8* (43), 18483–18488. https://doi.org/10.1039/c6nr05561c.

(40) Weng, G.; Tian, J.; Chen, S.; Xue, J.; Yan, J.; Hu, X.; Chen, S.; Zhu, Z.; Chu, J. Giant Reduction of the Random Lasing Threshold in CH3NH3PbBr3 Perovskite Thin Films by Using a Patterned Sapphire Substrate. *Nanoscale* **2019**, *11* (22), 10636–10645. https://doi.org/10.1039/c9nr00863b.

(41) Wiersma, D. S.; Cavalieri, S. A Temperature-Tunable Random Laser. *Nature* **2001**, *414* (6865), 708–709. https://doi.org/10.1038/414708a.

(42) Sapienza, R. Determining Random Lasing Action. *Nature Reviews Physics 2019 1:11* **2019**, *1* (11), 690–695. https://doi.org/10.1038/S42254-019-0113-8.

(43) Brenner, P.; Stulz, M.; Kapp, D.; Abzieher, T.; Paetzold, U. W.; Quintilla, A.; Howard, I. A.; Kalt, H.; Lemmer, U. Highly Stable Solution Processed Metal-Halide Perovskite Lasers on Nanoimprinted Distributed Feedback Structures. *Applied Physics Letters* **2016**, *109* (14), 141106. https://doi.org/10.1063/1.4963893.

(44) Palatnik, A.; Cho, C.; Zhang, C.; Sudzius, M.; Kroll, M.; Meister, S.; Leo, K. Control of Emission Characteristics of Perovskite Lasers through Optical Feedback. *Advanced Photonics Research* **2021**, *2* (12), 2100177. https://doi.org/10.1002/ADPR.202100177.

(45) Lei, J.; Qiu, S.; Yang, K.; Zhao, X. Research Status of Amplified Spontaneous Emission Sources Based on Doped Materials. *Journal of Physics: Conference Series* **2022**, *2248* (1). https://doi.org/10.1088/1742-6596/2248/1/012006.

(46) Chen, S.; Roh, K.; Lee, J.; Chong, W. K.; Lu, Y.; Mathews, N.; Sum, T. C.; Nurmikko, A. A Photonic Crystal Laser from Solution Based Organo-Lead Iodide Perovskite Thin Films. *ACS Nano* **2016**, *10* (4), 3959–3967. https://doi.org/10.1021/acsnano.5b08153.

(47) Roh, K.; Dang, C.; Lee, J.; Chen, S.; Steckel, J. S.; Coe-Sullivan, S.; Nurmikko, A. Surface-Emitting Red, Green, and Blue Colloidal Quantum Dot Distributed Feedback Lasers. *Optics Express* **2014**, *22* (15), 18800. https://doi.org/10.1364/oe.22.018800.

(48) Barnes, W. L.; Samuel, I. D. W.; Turnbull, G. A.; Andrew, P. Photonic Mode Dispersion of a Two-Dimensional Distributed Feedback Polymer Laser. *Physical Review B* **2003**, *67* (16), 165107. https://doi.org/10.1103/PhysRevB.67.165107.

(49) Zia, R.; Jiang, M.; Kurvits, J. A. Comparative Analysis of Imaging Configurations and Objectives for Fourier Microscopy. *JOSA A, Vol. 32, Issue 11, pp. 2082-2092* **2015**, *32* (11), 2082–2092. https://doi.org/10.1364/JOSAA.32.002082.

(50) Kozlov, V. G.; Bulović, V.; Burrows, P. E.; Forrest, S. R. Laser Action in Organic Semiconductor Waveguide and Double-Heterostructure Devices. *Nature 1997 389:6649* **1997**, *389* (6649), 362–364. https://doi.org/10.1038/38693.

(51) Henry, C. H.; Kazarinov, R. F.; Logan, R. A.; Yen, R. Observation of Destructive Interference in the Radiation Loss of Second-Order Distributed Feedback Lasers. *IEEE Journal of Quantum Electronics* **1985**, *21* (2), 151–154. https://doi.org/10.1109/JQE.1985.1072620.

(52) Li, S.; Witjaksono, G.; Macomber, S.; Botez, D. Analysis of Surface-Emitting Second-Order Distributed Feedback Lasers With Central Grating Phaseshift. *IEEE Journal on Selected Topics in Quantum Electronics* **2003**, *9* (5), 1153–1165. https://doi.org/10.1109/JSTQE.2003.819467.

(53) Reufer, M.; Feldmann, J.; Rudati, P.; Ruhl, A.; Müller, D.; Meerholz, K.; Karnutsch, C.; Gerken, M.; Lemmer, U. Amplified Spontaneous Emission in an Organic Semiconductor Multilayer Waveguide Structure Including a Highly Conductive Transparent Electrode. *Applied Physics Letters* **2005**, *86* (22), 221102. https://doi.org/10.1063/1.1938001.

(54) Andrew, P.; Turnbull, G. A.; Samuel, I. D. W.; Barnes, W. L. Photonic Band Structure and Emission Characteristics of a Metal-Backed Polymeric Distributed Feedback Laser. *Applied Physics Letters* **2002**, *81* (6), 954. https://doi.org/10.1063/1.1496497.

(55) Görrn, P.; Rabe, T.; Riedl, T.; Kowalsky, W.; Galbrecht, F.; Scherf, U. Low Loss Contacts for Organic Semiconductor Lasers. *Applied Physics Letters* **2006**, *89* (16), 161113. https://doi.org/10.1063/1.2360936.

(56) Kozlov, V. G.; Parthasarathy, G.; Burrows, P. E.; Khalfin, V. B.; Wang, J.; Chou, S. Y.; Forrest, S. R. Structures for Organic Diode Lasers and Optical Properties of Organic Semiconductors under Intense Optical and Electrical Excitations. *IEEE Journal of Quantum Electronics* **2000**, *36* (1), 18–26. https://doi.org/10.1109/3.817634.

(57) Yamamoto, H.; Oyamada, T.; Sasabe, H.; Adachi, C. Amplified Spontaneous Emission under Optical Pumping from an Organic Semiconductor Laser Structure Equipped with Transparent Carrier Injection Electrodes. *Applied Physics Letters* **2004**, *84* (8), 1401. https://doi.org/10.1063/1.1646730.

(58) Noll, R. J.; Macomber, S. H. Analysis of Grating Surface Emitting Lasers. *IEEE Journal of Quantum Electronics* **1990**, *26* (3), 456–466. https://doi.org/10.1109/3.52121.

(59) Streifer, W.; Scifres, D. R.; Burnham, R. D. Coupling Coefficients for Distributed Feedback Single- and Double-Heterostructure Diode Lasers. *IEEE Journal of Quantum Electronics* **1975**, *11* (11), 867–873. https://doi.org/10.1109/JQE.1975.1068539.

(60) Bonal, V.; Quintana, J. A.; Villalvilla, J. M.; Boj, P. G.; Díaz-García, M. A. Controlling the Emission Properties of Solution-Processed Organic Distributed Feedback Lasers through Resonator Design. *Scientific Reports 2019 9:1* **2019**, *9* (1), 1–10. https://doi.org/10.1038/s41598-

019-47589-4.

(61) Genoe, J. Coupled-Wave-Theory Distributed Feedback Lasers. https://github.com/jangenoe/Coupled-Wave-Theory_DFB-Lasers (accessed 2023-02-03).

For Table of Contents Use Only

TABLE OF CONTENTS GRAPHIC

Multimode Lasing in All-Solution-Processed UV-Nanoimprinted Distributed Feedback $MAPbI_3$ Perovskite Waveguides

Iakov Goldberg, Nirav Annavarapu, Simon Leitner, Karim Elkhouly, Fei Han, Niels Verellen, Tibor Kuna, Weiming Qiu, Cedric Rolin, Jan Genoe, Robert Gehlhaar, and Paul Heremans

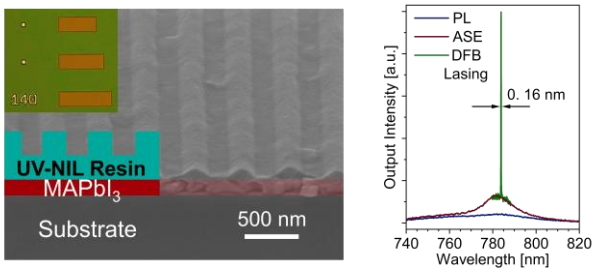

UV-Nanoimprint Lithography Enables High-Throughput Grating Fabrication for Perovskite-Based Lasers